



Mechanism of Water Inrush Through Fault Zones Using a Coupled Fluid–solid Numerical Model: A Case Study in the Beiyangzhuang Coal Mine, Northern China

Wenping Mu¹ · Xiong Wu¹ · Ruochen Deng¹ · Qian Hao¹ · Cheng Qian²

Received: 18 August 2019 / Accepted: 18 March 2020 / Published online: 18 May 2020
© Springer-Verlag GmbH Germany, part of Springer Nature 2020

Abstract

To better understand the mechanism of water inrush from fault zones, we investigated a typical inrush case from a coal mine in northern China, identified the water source and the role of fault zones, and analyzed the mechanical characteristics of the rock mass. We established a numerical model of fluid–solid coupling using finite difference methods based ideal elastic–plastic and Biot’s consolidation theories. The model considers softening effects caused by mine dewatering as well as the dynamic influence of mean principal stress and pore water pressure on fault zone permeability. It also simulates fault zone deformation, failure, and seepage under natural and disturbed-state conditions. The mechanism of water inrush through fault zones in a disturbed area was identified by comparing the deformation, failure, and seepage characteristics of fault zones with and without disturbance. The results show that deformation was concentrated at the bottom of the fault zone because of its naturally low strength, which created favorable conditions for water inrush. Softening of the media by mine dewatering also facilitated water inrush. Feedback effects between the fault zone and groundwater-enhanced permeability then led to groundwater bursting into the mine through the fault zone. This study provides an important framework for groundwater hazard prevention in similar mining areas.

Keywords Mine dewatering · Mechanical characteristics · Numerical simulation · Water–rock interaction · Seepage evolution

Introduction

Coal is the main energy resource in China and is expected to account for 50–70% of primary energy production for the foreseeable future (Gui and Lin 2016; Li and Wu 2019; Qian et al. 2018; Zhang 2005). Water inrush disasters are common in China’s underground coal mines because of complex geological and hydrogeological conditions, particularly in

northern China where karst aquifers underlie coal seams (Gui and Lin 2016; Li and Wu 2019; Shi and Singh 2001; Yin et al. 2016; Zhang et al. 2014). Although statistical information regarding water inrush events remains incomplete, approximately 80% of water inrush events in coal mines are known to be closely related to fault zones (Huang et al. 2010; Liu et al. 2017; Li and Wu 2019; Qian et al. 2018; Zhang 2005; Zhang et al. 2014), which are considered to play an important role during water inrush processes (Yin et al. 2015; Wu et al. 2004; Wu and Wang 2006). Most of these fault zones are impervious natural media that transform into water-conducting media under mining conditions (Li et al. 2002; Shi et al. 2017; Wu et al. 2004, 2011; Xu et al. 2012; Zhu et al. 2014). This type of water inrush is characterized by hysteresis, strong concealment, and capacity to inflict substantial harm (Wu et al. 2004, 2011; Zhu et al. 2014). Water inrush from fault zones into mines not only threatens safe production, but also presents environmental problems (Shi et al. 2017; Wu et al. 2004; Yin et al.

Electronic supplementary material The online version of this article (<https://doi.org/10.1007/s10230-020-00689-4>) contains supplementary material, which is available to authorized users.

✉ Xiong Wu
wuxiong@cugb.edu.cn

¹ School of Water Resources and Environment, China University of Geosciences (Beijing), Beijing 100083, China

² Construction Engineering Quality and Safety Supervision Station, Housing and Construction Bureau of Dapeng New District, Shenzhen 518119, China

2015; Zhang 2005; Zhu and Wei 2011). A better understanding of water inrush mechanisms is therefore required.

Fault zones often act as channels during mine water inrush events (Wu et al. 2019a, b; Yin et al. 2015; Zhang 2005; Zhou et al. 2018), yet the mechanism of this process remains poorly understood (Li and Wu 2019; Wu et al. 2019a, b; Zhang et al. 2017; Zhou et al. 2018; Zhu and Wei 2011). The occurrence and intensity of water inrush from a fault zone is controlled by its intrinsic properties, including stress state, fault displacement, rock mass structure, dip angle, cementation characteristics, and mineral composition (Li et al. 1999, 2011; Huang et al. 2010; Ma et al. 2016; Meng et al. 2012; Wu et al. 2004; Zhang 2005), and is also influenced by mining activities, aquiclude thickness, water yield property of aquifers, and hydraulic pressure of aquifers (Meng et al. 2012; Wu et al. 2004; Wu and Wang 2006; Zhang 2005; Zhang et al. 2014).

Three reasons are generally used to explain why fault zones often serve as a major passageway for water inrush. First, most fault zones are weak with high fissure ratios and low strength compared to surrounding rock, which significantly weakens their resistance to hydraulic pressure (Meng et al. 2001; Wu et al. 2004, 2019a, b). Second, interaction between groundwater and fault zones further weakens the fault zone strength while increasing permeability, leading to dissolution, softening, hydrostatic pressure, and subsurface erosion (Li et al. 1999, 2011; Qian et al. 2018; Zhang et al. 2014). A third cause is enhanced fault-zone permeability resulting from mining activity involving damage and fault activation (Zhang 2005; Zhang et al. 2014, 2015; Zhu et al. 2014; Zhu and Wei 2011), which has been verified by water pressure tests (Wang et al. 1997; Yin et al. 2015).

Nevertheless, qualitative analyses do not satisfactorily explain fault zone processes such as deformation, failure, and seepage flow, as well as their interrelationship. Quantitative methods used in previous studies include theoretical calculations, similar material simulations, and numerical simulations of fluid–solid coupling. Previous theoretical studies established based on mining rock mechanics and/or hydraulic fracturing theories (Shi and Singh 2001; Zhang 2005) analyzed stress variation, crack extension, and fault zone failure, and broadly discussed their effects on permeability (Bu and Mao 2009; Huang et al. 2010; Shi and Singh 2001; Yin et al. 2015; Zhang 2005). These theoretical calculations failed, however, to directly observe the phenomenon of fault zone deformation, failure, and seepage flow, and similar material simulations, though possible, remain inappropriate for practice (Li et al. 1997; Sun et al. 2015; Zhang et al. 2015, 2016, 2017; Zhu et al. 2017).

Numerical simulations of fluid–solid coupling using finite difference methods (FDM) or finite element methods (FEM) have been shown to overcome these shortcomings (Liu et al. 2017; Shi et al. 2017; Wu et al. 2004; Zhu et al. 2014; Zhou

et al. 2018; Zhu and Wei 2011). This approach is therefore widely used to explore the mechanisms of mine water inrush from fault zones on the basis of elastic–plastic or rheological mechanics and Biot’s consolidation theories (Liu et al. 2017; Wu et al. 2011; Yin et al. 2016; Zhu et al. 2014). Many studies have been performed using FLAC^{3D}, RFPA^{2D}-FLOW, and Comsol Multiphysics (Shi et al. 2017; Wu et al. 2011; Yin et al. 2016; Zhu and Wei 2011). The results show that a fault zone undergoes significant deformation and failure because of its low strength and stress redistribution under mining conditions (Bu and Mao 2009; Li et al. 2011; Liu et al. 2017; Shi et al. 2017; Wu et al. 2004, 2011; Yin et al. 2015, 2016; Zhang et al. 2015; Zhu et al. 2014), and that pore water pressure in aquifers increases because of additional stress (Wu et al. 2011; Zhang et al. 2016; Zhu et al. 2014). These changes induce groundwater bursts along fault zones into mines (Liu et al. 2017; Wu et al. 2004; Yin et al. 2016; Zhang et al. 2017). Few previous studies have reported the mechanism of water inrush from confined aquifers through fault zones disturbed by mine dewatering nor the evolution of fault zone hydraulic properties of natural vs. disturbed-state faults.

In this study, we consider these aforementioned questions using a typical water inrush event in a coal mine. We identified the water inrush source and the role of fault zones during the inrush, and analyzed the rock’s mass mechanical characteristics. We present a mathematical model of fluid–solid coupling based on ideal elastic–plastic and Biot’s consolidation theories that dynamically consider the effect of mean principal stress and pore water pressure on fault zone permeability. We apply the fluid–solid coupling numerical model to identify the water inrush mechanism through fault zones disturbed by mine dewatering.

Study Area

Geological and Hydrogeological Setting

The Beiyangzhuang coal mine is located in Yuxian County, Hebei Province, in northern China (Fig. 1), in a transition zone between semi-humid and semi-arid environments. Rainfall is concentrated between June and September with a long-term mean rainfall of ≈ 400 mm/year. The long-term average evaporation is ≈ 1600 mm/year. The geomorphology is dominated by an alluvial plain (Fig. 1), and the topography is relatively flat, with an elevation difference of about 140 m.

The study area is a synclinal structure with a dip angle on both limbs of $\approx 10^\circ$, and the axial plane of the syncline extends approximately W–E (Fig. 2). Large faults with throw of a few tens of meters are relatively infrequent, but small faults with < 10 m throws are fairly common. The main strata

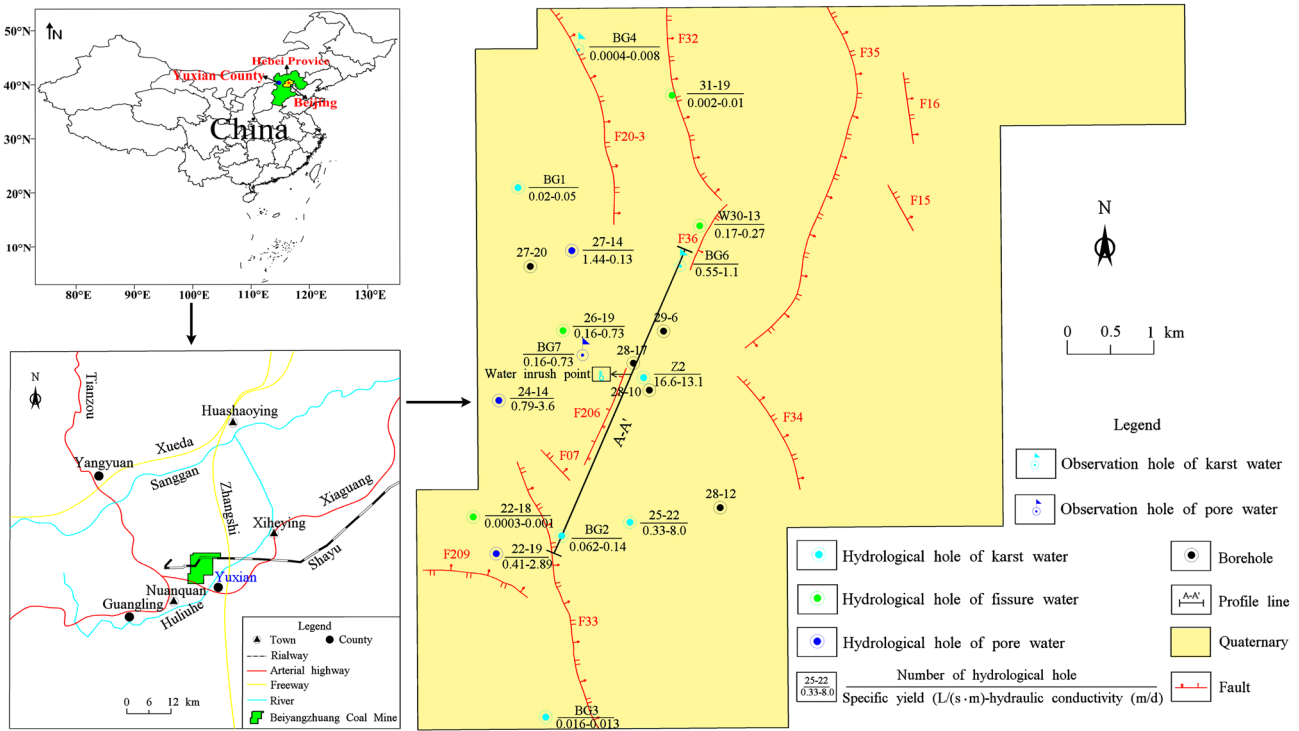


Fig. 1 Location and hydrogeological map of the study area

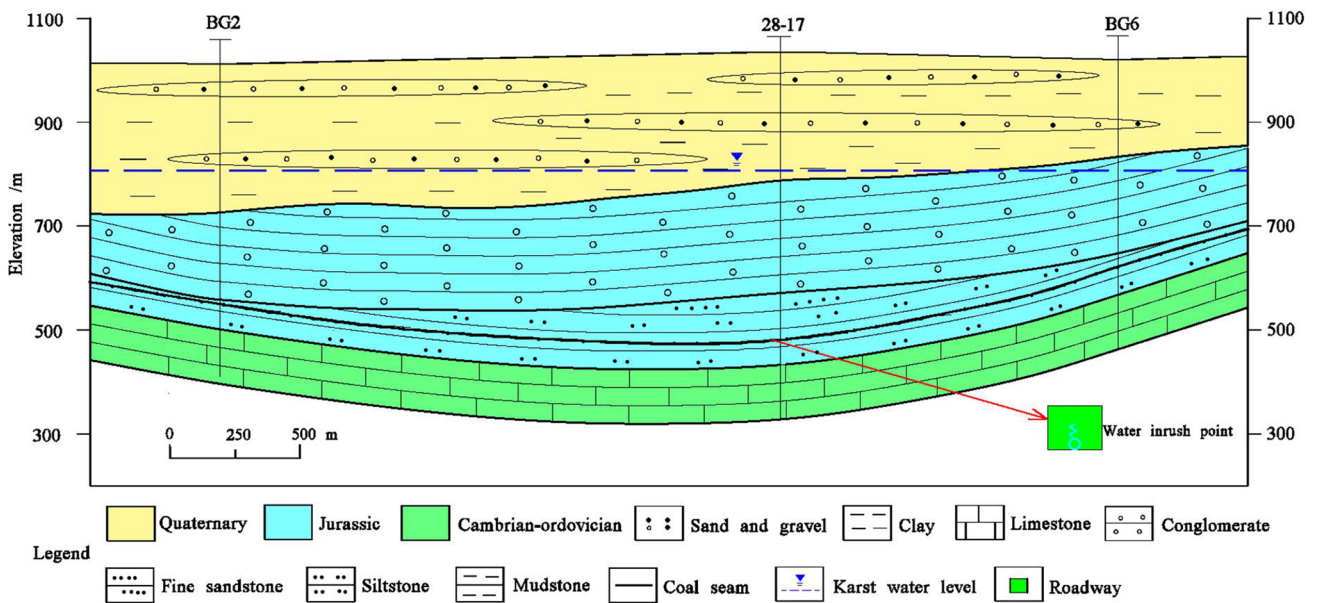


Fig. 2 A-A' hydrogeological profile in Fig. 1

include Cambrian–Ordovician carbonates, Jurassic clastic rocks, and Quaternary alluvial deposits. The coal seam occurs in the lower part of the Jurassic strata (Fig. 2).

The hydrogeological structure of the study area is vertically divided according to lithological associations into three aquifers (Cambrian–Ordovician karst aquifer, Jurassic

fissure aquifer, Quaternary pore aquifer), and two aquifuges (Jurassic aquifuge, Quaternary aquifuge) (Fig. 2).

The karst aquifer is characterized by a dual structure, where the upper part is thick-layered limestone and the lower part is thin-layered limestone. The thickness of the karst aquifer is ≈ 100 m (Fig. 2). The hydraulic conductivity ranges from 0.01 to 13.1 m/d, with an average of 3.2 m/day, which suggests significantly heterogeneous permeability. The specific yield ranges from 0.0004 to 16.6 L/(m·s), with an average of 2.5 L/(m·s) (Fig. 1), which suggests very heterogeneous water yield properties (Wu et al. 2006).

The fissure aquifer located in the upper part of the Jurassic strata is composed of 100–200 m of conglomerate (Fig. 2). The hydraulic conductivity ranges from 0.001 to 0.73 m/day, with an average of 0.25 m/day, and the specific yield ranges from 0.0003 to 0.17 L/(m·s), with an average of 0.07 L/(m·s) (Fig. 1). This suggests that the water yield property ranges from weak to medium. In general, the heterogeneity of the permeability and water yield property of the fissure aquifer is weaker than that of the karst aquifer.

The pore aquifer consists of interbedded sand and silty clay with a thickness ranging from 150 to 200 m (Fig. 2). The hydraulic conductivity ranges from 0.1 to 3.6 m/day, with an average of 1.8 m/day, and the specific yield ranges from 0.2 to 1.4 L/(m·s), with an average of 0.7 L/(m·s) (Fig. 1). The specific yield indicates that the water yield property varies from medium to strong. On the whole, the permeability and water yield property of the pore aquifer are relatively homogeneous.

The Jurassic aquifuge is located in the lower part of the Jurassic strata and its lithology includes mudstone, siltstone, and fine sandstone (Fig. 2). It therefore hydraulically

separates the karst and fissure aquifers. The Quaternary aquifuge consists of silty clay located in the bottom of the Quaternary strata (Fig. 2), hydraulically isolating the pore and fissure aquifers.

Conceptual Model

Water Inrush Process

The mine began dewatering using the no. 1 dewatering borehole near the F_1 fault on June 4, 2014, because of high hydraulic pressure (4.4 MPa) and the strong water yield property of the karst aquifer (Figs. 3, 4). The mine then also began dewatering using the no. 2 dewatering borehole near the F_1 fault on Aug. 31, 2014 (Figs. 3, 4) (Mu 2018). The average mine water yield was about 300 m³/h from June 4 to Sept. 26, 2014 (supplemental Fig. S-1). On Sept. 27, 2014, a large amount of water (about 550 m³/h) burst into the roadway from the coal wall around the no. 2 dewatering boreholes, and the mine’s water yield quickly increased to the maximum (about 2200 m³/h) on Nov. 2, 2014 (Fig. S-1) (Mu 2018). A water gate wall was used to control the water hazard on Nov. 3, 2014, which reduced the mine’s water yield to ≈ 1900 m³/h, and it roughly remained at this level until July 6, 2015 (Fig. S-1). The water inrush pathway was blocked by grouting between July 7 and Aug. 10, 2015, causing the mine’s water yield to quickly drop to ≈ 40 m³/h (Fig. S-1).

The drainage stage was divided into three stages to embody the difference ways groundwater entered the mine (Fig. S-1): the dewatering stage (June 4, 2014–Sept. 26,

Fig. 3 Conceptual model of water inrush through fault zones

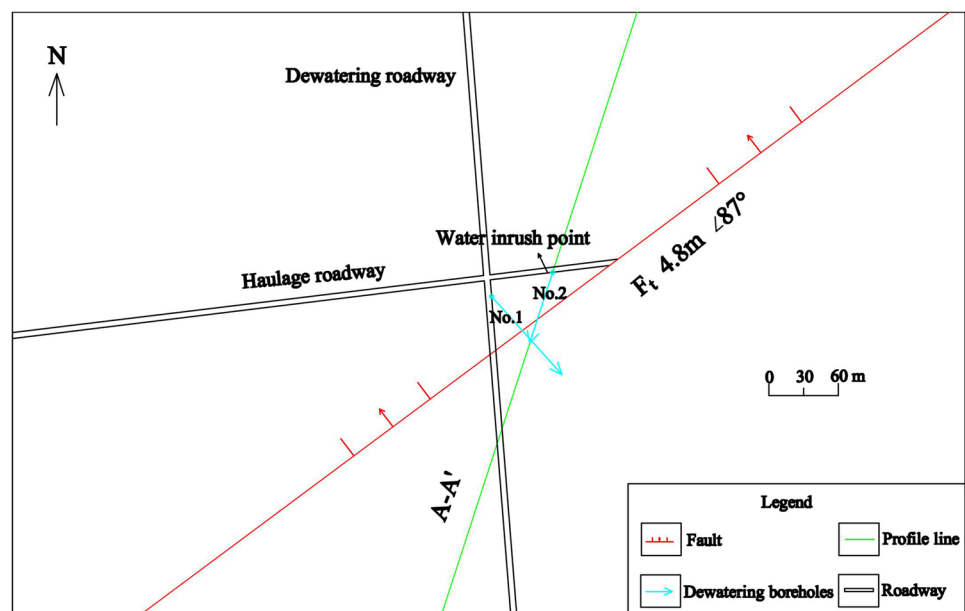
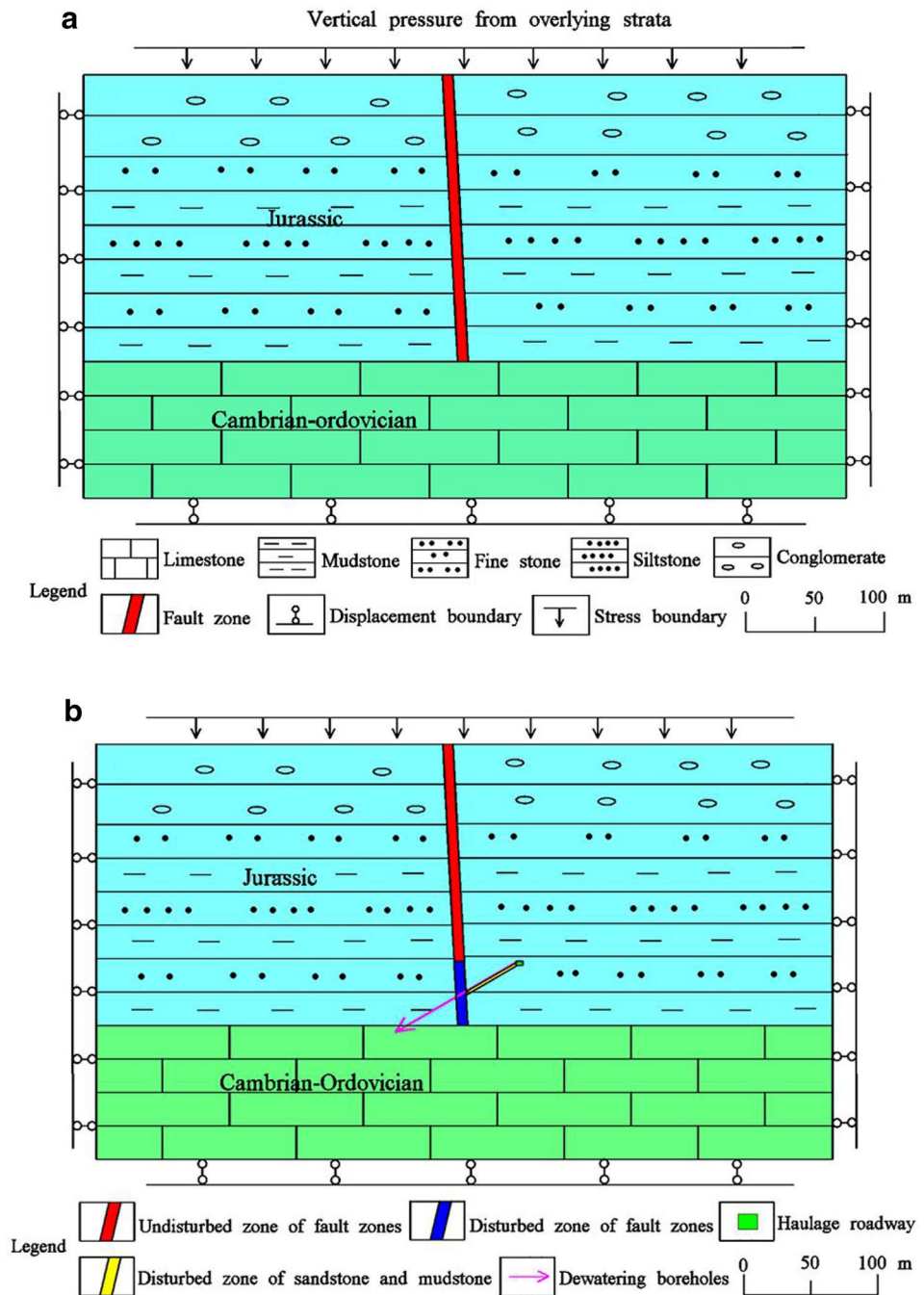


Fig. 4 A-A' Engineering geological profile in Fig. 3 in the **a** natural state and **b** disturbed state



2014), the water inrush (Sept. 27, 2014–July 6, 2015), and the water-level recovery stage (July 7, 2015–Aug. 10, 2015).

Water Source Identification

The planar distance of observation hole BG6 from the water inrush point was ≈ 1500 m, while the planar distance of observation hole BG7 from the inrush point was ≈ 600 m (Fig. 1). BG6 was intended to measure the karst water regime during the mine water inrush process, and was used

to analyze the influence of mine water inrush on the karst water level. Similarly, BG7 was intended to measure the pore water regime during the inrush process, and was used to analyze the influence of the inrush on the karst water level.

A strong negative correlation was observed between the karst water regime at observation hole BG6 and the variation of water yield of mine during the water inrush process (Fig. S-1) (Wu et al. 2019a, b). The water level at the observation hole decreased by 22 m during the inrush and increased by 21 m after the grouting. This indicates that karst water was

the main source of the water inrush (Fig. S-1). In addition, the response of the karst water level at BG6 was measured in three pressure tests for the water gate wall (Fig. S-1).

In contrast, no correlation was observed between the pore water regime at BG7 and the change in mine water yield during the inrush process (Fig. S-1). The pore water regime at the observation hole was influenced by atmospheric precipitation, groundwater exploitation for agriculture, and snow-melt (Wu et al. 2019a, b), which suggests that pore water does not contribute substantially to water inrush (Mu 2018).

A Piper diagram was used to classify the hydrochemical types of the water samples. The pore water is mainly $\text{HCO}_3\text{-Na}$ type, the fissure water is mainly $\text{HCO}_3\text{-Na}$ and $\text{HCO}_3\text{-Cl-Na}$ types, and the karst water is mainly $\text{HCO}_3\text{-Cl}$ and $\text{HCO}_3\text{-SO}_4$ types (Fig. S-2). The hydrochemical facies of water samples from the water inrush point is $\text{HCO}_3\text{-SO}_4$ type, clearly resembling the karst water in the Piper diagram (Wu et al. 2019a, b). In combination with groundwater level measurements, we can infer that the karst aquifer below the coal seam was the water inrush source. The hydrochemical characteristics also indirectly confirm that the hydraulic connections are not close among the three aquifers (supplemental Fig. S-2).

Role of the Fault

The exposure site of the F_1 fault is ≈ 50 m from the no. 2 dewatering boreholes in the roadway, and its role in the water inrush process was roughly analyzed (Figs. 3, 4). The average throw of the F_1 fault is 4.8 m and the fault zone width is 4.5 m. It is a normal fault and the lithology of each wall includes fine sandstone, siltstone, and mudstone (Figs. 3, 4). The fault zone is naturally impermeable, according to roadway exposure. No water was observed when the no. 1 dewatering borehole exposed the fault in late May 2014. But, a large amount of water was observed when the no. 2 dewatering borehole exposed the fault at the end of August 2014, indicating that the hydraulic property of the fault zone changed from impermeable to water-conducting. In other words, fault activation occurred near the end of August 2014.

The coal near the inrush points was unmined before the end of August 2014 or late May 2014, so the fault activation was not mining related. Mine dewatering was carried out near the fault from late May 2014 to the end of August 2014 (Figs. 3, 4). Therefore, the fault activation was possibly related to the mine dewatering, based on the following reasoning: the fault zone intersects the dewatering boreholes in the Jurassic aquifuge below the coal seam (Figs. 3, 4). The groundwater in the borehole permeates the fault zone under high hydraulic pressure. The fault zone is composed of clay minerals, including an illite-montmorillonite mixed-layer, illite, and kaolinite (Mu 2018). Due to the high

hydrophilicity of clay minerals, the strength of the fault zone was therefore significantly reduced, which activated the fault and enhanced the fault zone's permeability. The Jurassic aquifuge contains the same clay minerals and the softening induced the karst water to flow along the fault and failure zones in the rock surrounding the dewatering boreholes, and eventually burst into the roadway. When the grouting cut off the connection between the fault zone and karst aquifer, the water yield of the mine sharply decreased (Fig. S-1), verifying the role that fault zones play in water inrush passage.

Materials and Methods

Sample Collection and Testing

Twenty-five samples were collected from the lower part of the Jurassic strata because the mechanical properties of this layer are closely related to water inrush from the coal floor. Among these samples, eight were fine sandstone, eight were siltstone, and nine were mudstone (Fig. S-3). The samples were tested for physical and mechanical parameters including bulk density, porosity, water absorption, cohesion, internal friction angle, and uniaxial compressive strength (UCS). These test results are listed in Table 1.

Methods Overview

Fault zones are generally classified as fracture zones and influenced zones from inside to outside. Fracture zones are composed of fine particles, while influenced zones are composed of rock blocks and fissure networks (Meng et al. 2001; Zhang et al. 2014; Zhou et al. 2018). Rock mass structures of fault zones are therefore successively structurally classified as granular and cataclastic from inside to outside, respectively (Zhou et al. 2018). Although a fault zone is relatively heterogeneous compared with soil mass, it can still be approximately regarded as an equivalent porous media at the macroscopic scale (Wu et al. 2011). On this basis, we used a mathematical model of fluid–solid coupling to describe the deformation, failure, and seepage of fault zones.

The coupled model consists of the ideal elastic–plastic and Biot's consolidation models. Volumetric strain plays a bridge role in the coupled model. The effects of average principal stress and pore water pressure on the fracture zone permeability are considered by coupling the models. The FLAC^{3D} (Fast Lagrangian analysis of continua in three dimensions) software was then employed using finite difference methods to perform numerical simulations of fluid–solid coupling based on the conceptual model of water inrush, rock physics and mechanics test results, and mathematical model of the fluid–solid coupling.

Table 1 Test results of physical and mechanic of rock mass

Sample	Lithology	Density (kN/m ³)	Porosity (%)	Water absorption (%)	UCS ^a (MPa)	Internal friction angle (°)	Cohesion (MPa)
1	Fine sandstone	22	14.0	10.9	17.1	30	4.7
2		23	13.8	6.9	20.1	32	5.8
3		23	12.8	5.7	10.5	29	3.5
4		25	5.8	4.4	12.7	36	4.2
5		21	19.3	21.0	15.3	33	4.7
6		22	14.8	8.1	23.4	31	6.2
7		24	10.6	34.0	21.6	35	5.1
8		24	10.8	13.9	14.1	30	4.2
9	Siltstone	27	2.0	1.2	60.9	36	14.5
10		23	12.3	8.0	36.2	35	7.1
11		24	10.2	32.6	11.8	30	4.2
12		23	11.0	6.6	16.1	31	4.8
13		25	5.6	3.6	18.1	35	6.0
14		23	13.9	11.7	10.3	32	4.2
15		25	7.4	16.1	19.6	28	3.9
16		24	11.6	12.2	11.0	31	4.4
17	Mudstone	24	13.8	5.1	13.1	34	4.4
18		26	1.6	5.9	26.0	33	7.6
19		23	11.7	8.8	19.1	32	5.3
20		24	11.4	4.5	23.7	37	5.9
21		23	27.8	24.0	19.3	31	3.8
22		23	11.3	28.5	16.5	32	5.1
23		23	19.2	5.6	12.7	31	4.1
24		24	10.8	13.9	14.1	30	4.2
25		24	10.5	29.3	13.0	32	4.3

^aUniaxial compressive strength

Mathematical Model of Fluid–Solid Coupling

Ideal Elastic–Plastic Model

According to Hooke's law, the relationship between principal stress increment and principal strain increment in the elastic stage is expressed by (Mu 2018):

$$\begin{cases} \Delta\sigma_1 = \alpha_1 \Delta e_1^e + \alpha_2 (\Delta e_2^e + \Delta e_3^e) \\ \Delta\sigma_2 = \alpha_1 \Delta e_2^e + \alpha_2 (\Delta e_1^e + \Delta e_3^e) \\ \Delta\sigma_3 = \alpha_1 \Delta e_3^e + \alpha_2 (\Delta e_1^e + \Delta e_2^e) \end{cases} \quad (1)$$

where $\Delta\sigma_i (i = 1, 3)$ is the principal stress increment, $\Delta e_i^e (i = 1, 3)$ is the principal strain increment in the elastic stage, and α_1 and α_2 are related to bulk modulus and shear modulus, and are defined by:

$$\alpha_1 = B + (4/3)S, \quad \alpha_2 = B + (2/3)S \quad (2)$$

where B and S are the bulk modulus and shear modulus, respectively. The Mohr–Coulomb yield function (f_s) is defined as:

$$f_s = \sigma_1 - \sigma_3 N_\phi + 2c N_\phi \quad (3)$$

where σ_1 and σ_3 are the maximum principal stress and minimum principal stress, respectively, c is cohesion, and N_ϕ is the parameter related to internal friction angle defined as:

$$N_\phi = \frac{1 + \sin \phi}{1 - \sin \phi} \quad (4)$$

where ϕ is the internal friction angle. The shear potential function (g^s) is defined as (Mu 2018):

$$g^s = \sigma^t - \sigma_3 N_\phi \quad (5)$$

where σ^t is the tensile strength, and N_ϕ is a parameter which is related to internal friction angle, which is defined as follows:

$$N_\varphi = \frac{1 + \sin \varphi}{1 - \sin \varphi} \tag{6}$$

where φ is a parameter related to dilation angle. When the material is in shear yield, the strain increment in the plastic stage is determined according to the shear potential function and plastic flow rule (Mu 2018):

$$\Delta e_i^p = \lambda^s \frac{\partial g^s}{\partial \sigma_i} \quad i = 1, 3 \tag{7}$$

where Δe_i^p is the strain increment in the plastic stage and λ^s is the shear plasticity factor. The total principal strain increment includes the strain increment in the elastic stage and the plastic strain increment in the plastic stage:

$$\Delta e_i = \Delta e_i^e + \Delta e_i^p \quad i = 1, 3 \tag{8}$$

where Δe_i is the total principal strain increment. The relationship between the principal stress increment and total principal strain increment is obtained from Eqs. (7) and (8) applied to Eq. (1):

$$\begin{cases} \Delta \sigma_1 = \alpha_1 \Delta e_1 + \alpha_2 (\Delta e_2 + \Delta e_3) - \lambda^s (\alpha_1 - \alpha_2 N_\varphi) \\ \Delta \sigma_2 = \alpha_1 \Delta e_2 + \alpha_2 (\Delta e_1 + \Delta e_3) - \lambda^s \alpha_2 (1 - N_\varphi) \\ \Delta \sigma_3 = \alpha_1 \Delta e_3 + \alpha_2 (\Delta e_1 + \Delta e_2) - \lambda^s (-\alpha_1 N_\varphi + \alpha_1) \end{cases} \tag{9}$$

Biot’s Consolidation Model

According to Darcy’s law, the seepage velocity of groundwater is described by:

$$v_i = \frac{K}{\rho_w g} \frac{\partial (p + \rho_w g z)}{\partial x_i} \tag{10}$$

where v_i is the seepage velocity, p is the pore water pressure, K is the hydraulic conductivity, ρ_w is the groundwater density, z is the elevation head, and g is the gravitational acceleration. The continuity equation of groundwater is (Wang et al. 2018):

$$\frac{\partial V_i}{\partial x_i} = \frac{\partial \zeta}{\partial t} \quad (i = 1, 3) \tag{11}$$

where ζ is the volume variation of groundwater in unit volume of the aquifer. The constitutive equations of groundwater are defined by (Wang et al. 2018):

$$\frac{\partial \zeta}{\partial t} = \frac{1}{M} \frac{\partial p}{\partial t} + \alpha \frac{\partial \varepsilon_V}{\partial t} \tag{12}$$

where α is the Biot consolidation coefficient, M is the Biot modulus, and ε_V is the volumetric strain. The volumetric strain is a link for the coupling of the seepage field and stress field:

$$\varepsilon_V = \sum_{i=1}^3 \varepsilon_i \tag{13}$$

where ε_i is the total principal strain.

Relationship Among Permeability, Stress, and Pore Pressure

Many studies have shown that fault zone permeability is influenced by principal stress and pore water pressure (Wu et al. 2011). In general, there is a negative correlation between hydraulic conductivity and principal stress of fault zones because of compaction, and their relationship is frequently described by a negative exponential function (Li and Wu 2019; Li et al. 2011; Wu et al. 2011; Zhu and Wei 2011; Zhu et al. 2014). However, there is a positive correlation between hydraulic conductivity and pore water pressure of fault zones because of wedging action (Li et al. 2002, 2011). A natural exponential function model was used to describe the relationship among hydraulic conductivity, mean principal stress, and pore water pressure for fault zones on the basis of the above analysis (Wu et al. 2011; Zhu et al. 2014):

$$K = K_0 e^{-\alpha(\sigma_m - p)} \tag{14}$$

where σ_m is the mean principal stress, α is a fitting parameter, p is the pore water pressure, and K is the hydraulic conductivity when the mean principal stress is equal to pore water pressure. The mean principal stress is defined as:

$$\sigma_m = \frac{1}{3} \sum_{i=1}^3 \sigma_i \tag{15}$$

where $\sigma_i (i = 1, 3)$ is principal stress. According to the time of fault activation (about 90–100 days), the parameters in Eq. (14) are identified by application of parameter inversion. In Eq. (14), a is equal to 1.5, and K_0 is equal to 1.45×10^{-2} cm/s.

Numerical Model

Geological Structure

The geologic structure model is naturally divided into four groups based on their lithologic features: the Cambrian–Ordovician limestone, the Jurassic sandstone and mudstone, the Jurassic conglomerate, and the fault zone (Fig. 4a). To embody the softening effect of the groundwater on the rock mass, the Jurassic sandstone and mudstone as well as the fault zone, were further divided into disturbed and undisturbed zones (Fig. 4b), while the other groups remained the same. The model was therefore divided into six groups in the disturbed state.

Parameters and Boundary Conditions

The physical and mechanical parameters of the model in the natural state were determined using laboratory tests and field investigations (Table 2). Similarly, the physical and mechanical parameters of the model were determined in the disturbed state. The mechanical parameters of the disturbed rock mass were clearly weaker than those of the same rock mass in the natural state (Table 3).

According to our water inrush source analysis, the inrush was only related to the karst aquifer, so to simplify calculations, the seepage model considers only the karst aquifer; the other materials were regarded as impermeable media, except for the fault zone and the disturbed Jurassic rock mass.

The hydraulic conductivity of the karst aquifer was measured from the pumping test to be 5.78×10^{-3} cm/s. The natural hydraulic conductivity of the fault zone was 1.89×10^{-8} cm/s, according to the hydrogeological tests and field investigation. The hydraulic conductivity of the disturbed rock mass in the fault zone was dynamically calculated using Eq. (14). The lateral and bottom boundaries in the mechanical model were defined as the boundary with a normal displacement of 0 m (Fig. 4). The top boundary was defined as a stress boundary to simulate gravitational stress of the overlying strata (Fig. 4), and a vertical stress of 8.8 MPa was calculated, based on the unit weight and

thickness of the overlying strata including the Jurassic conglomerate and Quaternary alluvial deposits (Fig. 2).

The right and south boundaries in the seepage model were defined as the fixed pore pressure, while the other boundaries were regarded as confining boundaries. The pore water pressure in the left and right boundaries was identified according to the pore water pressure of the observation well before mine dewatering and ranged from 4.4 to 5.4 MPa.

Simulation Scheme

Understanding the evolution of hydraulic properties from the natural to the disturbed state is the key to identifying the mechanism of water inrush through fault zones. We designed two simulation schemes based on the conceptual model, one for the natural state and the other for the disturbed state. Comparing the deformation, failure, and seepage of fault zones in both states should reveal the inrush mechanism of the fault zone

The initial seepage is believed to have begun in late May, 2014. The seepage time in the natural state simulation was set at 120 days, slightly exceeding the time of fault activation (about 90–100 days). The seepage time in the disturbed state was set at 160 days, to exceed the actual delay of mine water inrush (about 120–130 days). The model parameters

Table 2 Physical and mechanical parameters of rock mass in the natural state

Lithology	Bulk density (kN/m ³)	Elastic modulus (GPa)	Poisson ratio	Internal friction angle (°)	Cohesion (MPa)	Tensile strength (MPa)
Limestone	27	20.0	0.26	38	1.5	9.0
Conglomerate	26	7.0	0.28	35	0.2	0.6
sandstone and mudstone ^a	25	5.0	0.30	35	0.4	2.0
Fault zones	23	4.5	0.32	25	0.05	0.003

^aInterbedded sandstone and mudstone

Table 3 Physical and mechanical parameters of rock mass in the disturbed state

Lithology	Bulk density (KN/m ³)	Elastic modulus (GPa)	Poisson ratio	Internal friction angle (°)	Cohesion (MPa)	Tensile strength (MPa)
Limestone	27	20.0	0.26	38	1.2	9.0
Conglomerate	26	7.0	0.28	35	0.2	0.6
Sandstone and mudstone ^a	25	5.0	0.28	35	0.4	2.0
Disturbed zone of surrounding rock ^b	25	1.0	0.33	19	0.6	0.04
Undisturbed zone of fault zones	23	4.5	0.32	25	0.05	0.003
Disturbed zone of fault zones	23	0.8	0.35	8	0.005	0.0

^aInterbedded sandstone and mudstone

^bSurrounding rock is interbedded sandstone and mudstone

were calibrated by model inversion, based on the time of fault activation.

Results and Discussion

Mechanical Characteristics of the Rock Mass

The porosity of the fine sandstone ranges from 5.8 to 19.3%, averaging 12.7%; that of the siltstone ranges from 2.0 to 13.9%, averaging 9.3%; and that of the mudstone ranges from 1.6 to 27.8%, averaging 14.0%. The porosity was therefore relatively developed, which indicates relatively poor cementation.

The water absorption of the fine sandstone ranges from 4.4 to 36%, with an average of 13.1%; that of siltstone ranges from 1.2 to 32%, averaging 11.5%; and that of the mudstone ranges from 4.5 to 29.3%, averaging 14.0%. These percentages are relatively large, due to the strong hydrophilicity of the clay minerals.

The UCS of the rocks is influenced by the poor cementation and strong hydrophilicity. The UCS of the fine sandstone ranges from 10.5 to 23.4 MPa, with an average of 16.9 MPa; that of the siltstone ranges from 10.3 to 60.9 MPa, averaging 23 MPa; and that of the mudstone ranges from 13 to 26 MPa, with an average of 17.5 MPa. The UCS is less than 30 MPa, which is characteristic of soft rock. The softening coefficient of rocks ranges from 0.25 to 0.42, which suggests that water plays a critical role in strength deterioration.

Deformation, Failure, and Seepage Characteristics

Natural state

The shear strain increment at the bottom of the fault zone was considerably larger than in other areas of the natural state simulation (Fig. 5). The volume strain increment and horizontal displacement showed the same trend (Fig. 6). The deformation slowly increases with seepage time, and the deformation concentration of fault zones presents a punctiform distribution (Fig. 7). Only the fault zone bottom undergoes failure, whereas other areas of the fault zone do not (Fig. 8).

The deformation and failure are concentrated at the bottom of the fault zone because of its low strength in the natural state, which provides favorable conditions for water inrush along fault zones. Groundwater from the karst aquifer moves slowly along the fault zone under high pore water pressure, with a seepage velocity of 1.5 cm/day (Fig. 9). The fault zone can therefore be regarded as a naturally fairly impermeable medium.

Disturbed State

The shear strain increment of the disturbed zone of the fault zone was substantially larger than in the other areas in the disturbed state, and about 40 times greater than the natural state (Fig. 10). The volume strain increment and horizontal displacement also show the same relationship, and were

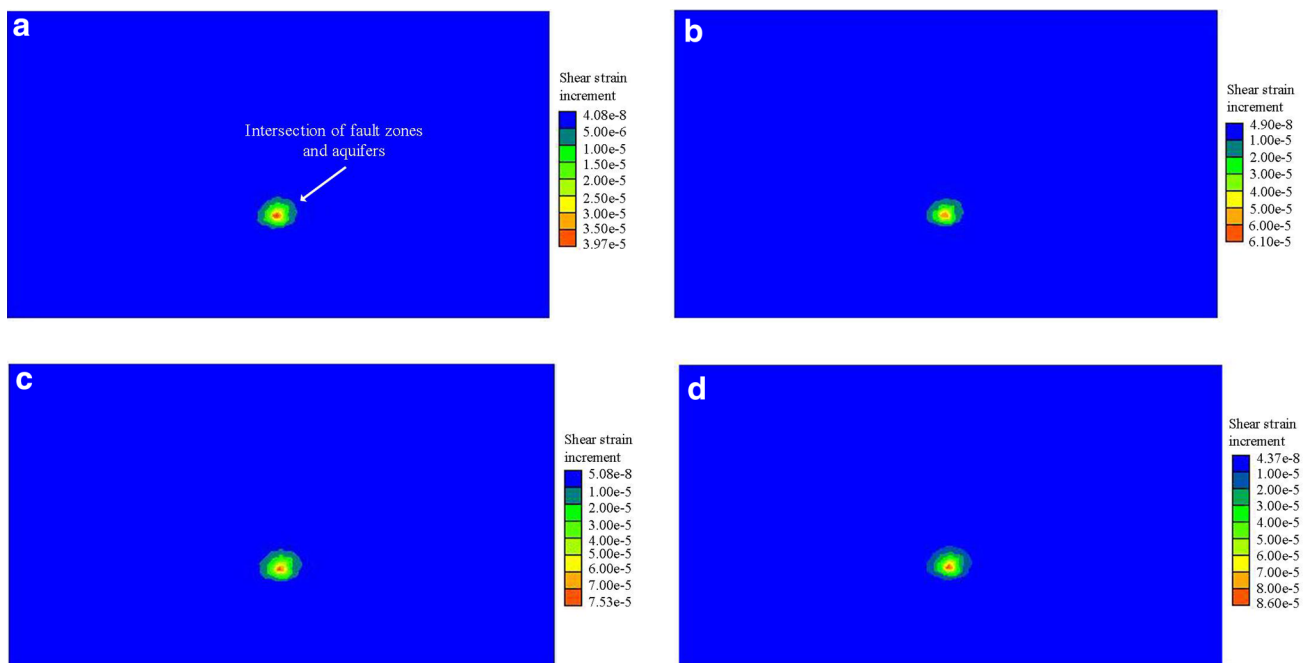


Fig. 5 Shear strain increment for different seepage times in the natural state: **a** 30 days; **b** 60 days; **c** 90 days; **d** 120 days

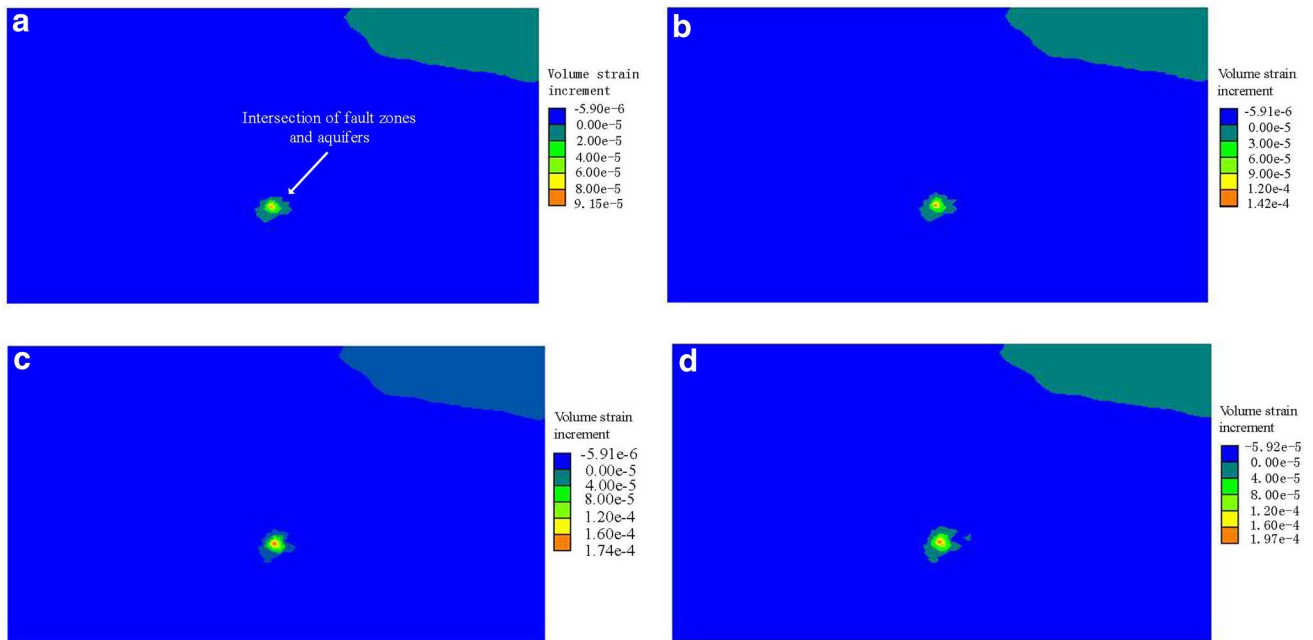


Fig. 6 Volume strain increment for different seepage times in the natural state: **a** 30 days; **b** 60 days; **c** 90 days; **d** 120 days

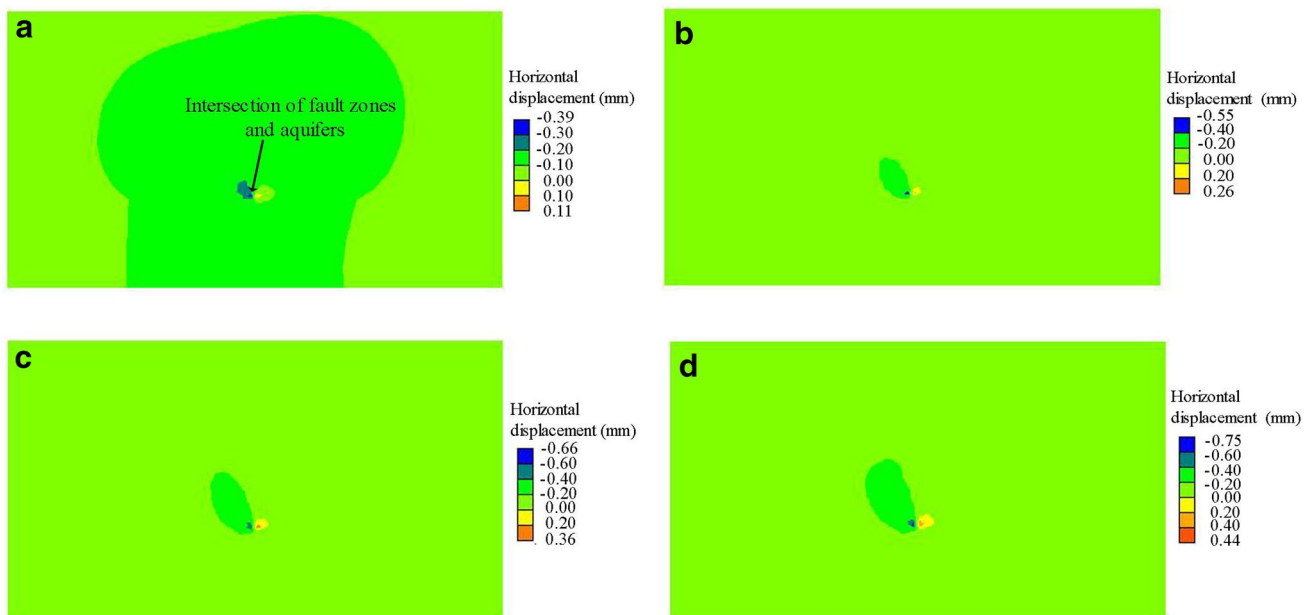


Fig. 7 Horizontal displacement for different seepage times in the natural state: **a** 30 days; **b** 60 days; **c** 90 days; **d** 120 days

enhanced by about an order of magnitude (Fig. 11). The deformation concentration of fault zones presents a zonal distribution (Fig. 12). Note that the fault zone was in a state of volume expansion, based on the volume strain increment in the disturbed state, which shows that the porosity of fault zones increased (Liu et al. 2009; Wang et al. 2001).

The failure of the fault zone initiated in the bottom of the disturbed area, and gradually developed upward (Fig. 13). The entire disturbed zone underwent failure due to the pore water pressure (Liu et al. 2017). The natural deformation and failure characteristics of the fault zone were enhanced in the disturbed state (Figs. 7, 8, 12, 13).

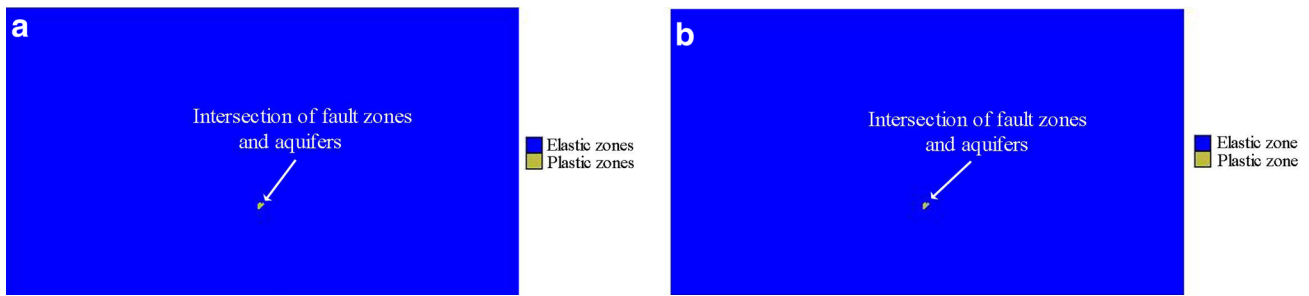


Fig. 8 Plastic zones for different seepage times in the natural state: **a** 30 days; **b** 120 days

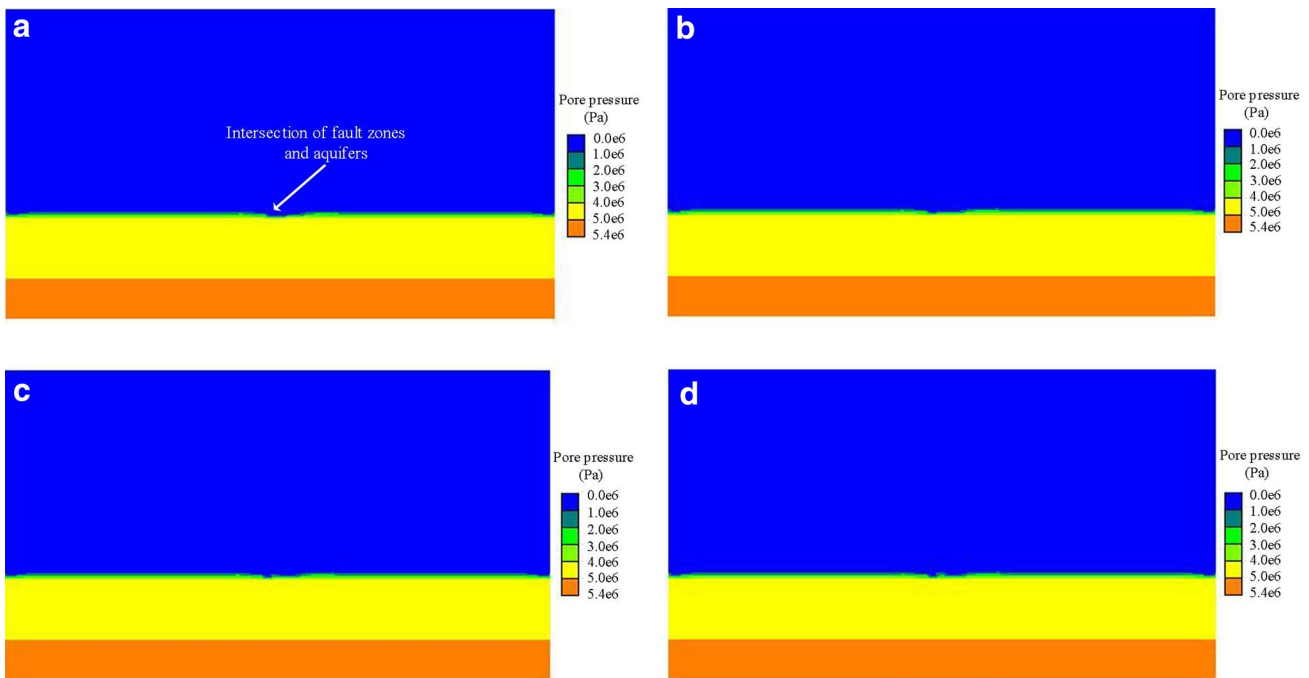


Fig. 9 Pore water pressure for different seepage times in the natural state: **a** 30 days; **b** 60 days; **c** 90 days; **d** 120 days

Groundwater moved upward 3 m along the fault zone after 30 days (Figs. 14a, S-4), 6.5 m after 60 days (Figs. 14b, S-4), 11 m after 90 days (Figs. 14c, S-4), and 16.2 m after 120 days (Figs. 14d, S-4). This indicates that the seepage velocity gradually increased with time, which fully embodied the groundwater’s wedge action. The hydraulic gradient of groundwater was ≈ 20 and fine particles in the fault zone were removed under the high seepage pressure after the fault zone fails (Jiang et al. 2013; Ma et al. 2016; Zhang et al. 2014). The seepage deformation accelerated groundwater movement along the fault zone (Figs. 14e, f, S-4).

The rock surrounding dewatering boreholes can fail due to softening and hydraulic fracturing (Fig. 13e, f), which leads to a significant increase in the media permeability (Li and Wu 2019; Wang et al. 2001; Yin et al. 2015). Groundwater from the karst aquifer bursts into the mine along the fault

zone and weak areas in the surrounding rock (supplemental Fig. S-4).

The time of water inrush could have been predicted by monitoring the hydraulic pressure at points in the fault zone and the rock surrounding the dewatering boreholes. The simulation results indicate an inrush delay of about 150 days (Fig. S-4), slightly longer than the actual delay time (about 120–130 days). This confirms that the numerical model of fluid–solid coupling is reasonable for this study.

Water Inrush Mechanism

The deformation and failure were concentrated at the bottom of the fault zone because of its natural weakness there (Figs. 7, 8). The mechanical properties of the fault zone are very sensitive to water because of the strong hydrophilicity

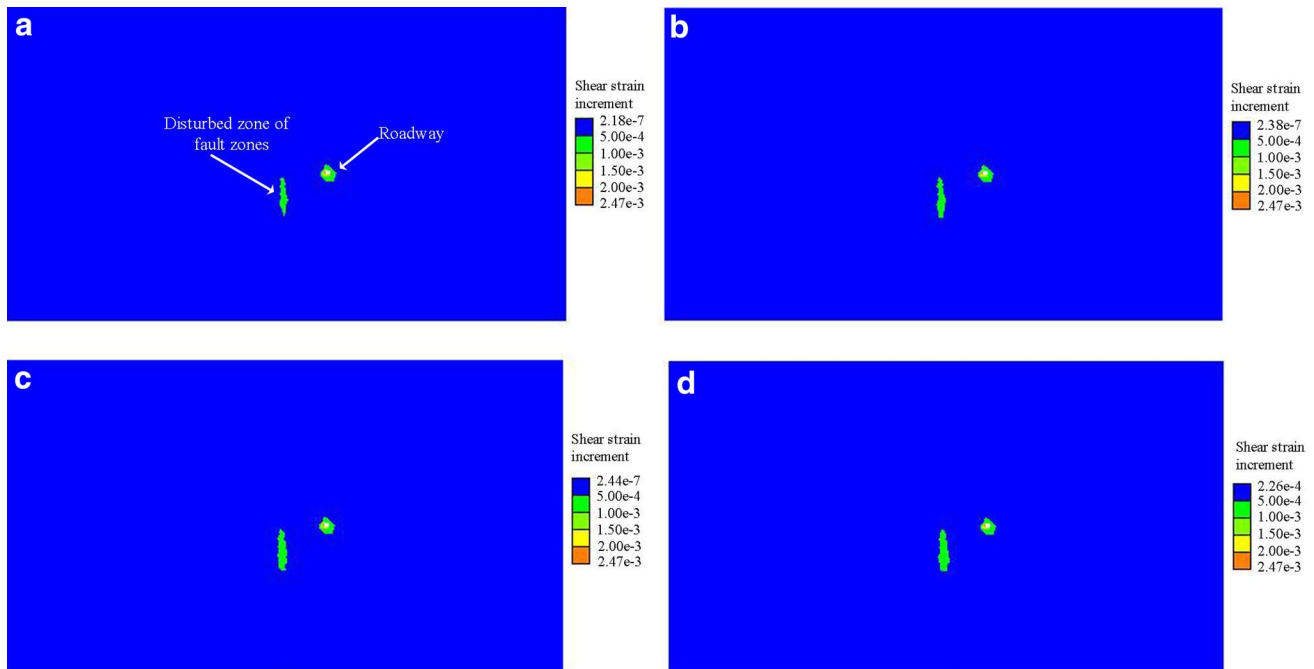


Fig. 10 Shear strain increment for different seepage times in the disturbed state: **a** 30 days; **b** 60 days; **c** 90 days; **d** 120 days

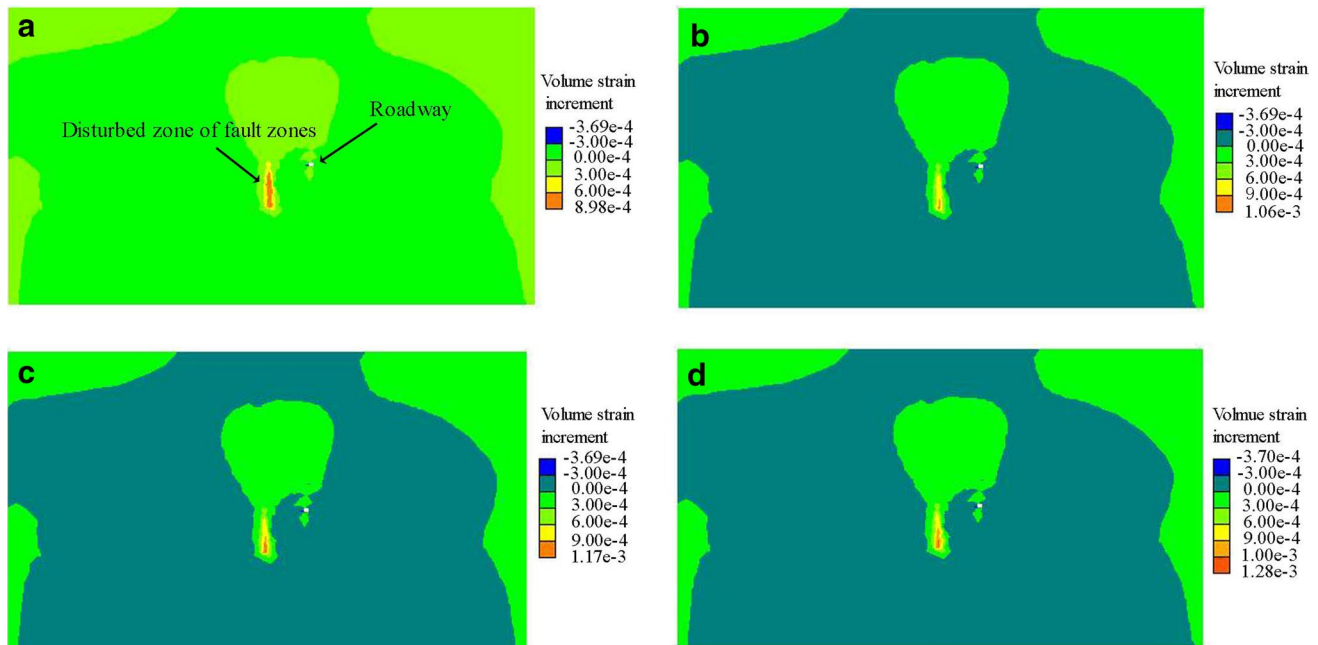


Fig. 11 Volume strain increment for different seepage times in the disturbed state: **a** 30 days; **b** 60 days; **c** 90 days; **d** 120 days

of the clay minerals, such as the illite-montmorillonite mixed-layer and illite, which created favorable conditions for water inrush (Mu 2018).

The maximum principal stress of the fault zone decreased substantially in the disturbed state due to softening (Figs. S-5, S-6), which loosened the material (Wu et al. 2011),

which was already in a state of volume expansion (Wu et al. 2004). This enhanced the fault zone's permeability, causing groundwater to enter it. The pore water pressure then further enhanced the fault zone's permeability (Fig. 15) and initiated failure because of the reduced effective stress (Liu et al. 2017). This also promoted upward groundwater movement.

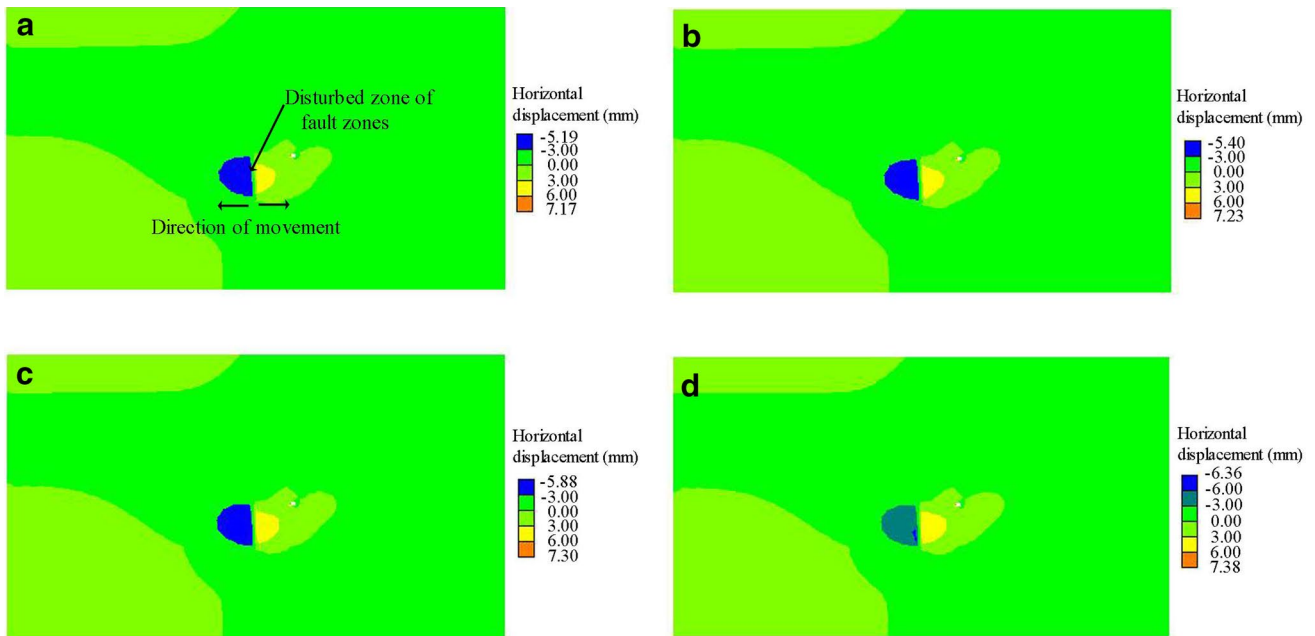


Fig. 12 Horizontal displacement for different seepage times in the disturbed state: **a** 30 days; **b** 60 days; **c** 90 days; **d** 120 days

Fine particles were removed under the high seepage pressure after the fault zone failed, which further increased permeability (Jiang et al. 2014; Ma et al. 2016; Zhang et al. 2014) and groundwater movement along the fault zone (Fig. 14e, f).

The hydraulic properties of the fault zone transformed from an impermeable medium in the natural state to a water-conducting medium, causing rapid movement of groundwater along the fault zone (Figs. 13, S-4) (Qian et al. 2018). The rock surrounding the dewatering boreholes also underwent failure because of the low strength and softening (Fig. 13) (Yin et al. 2016). Groundwater eventually burst into the mine along the fault zone and where the surrounding rock failed (Fig. S-4).

An essential component of the water inrush was the feedback effect. First, hydration between media and water led to strength deterioration when groundwater in the dewatering boreholes encountered the fault zone. Strength deterioration then reduced the maximum principal stress and volume expansion, which enhanced fault zone permeability, which in turn further increased the pore water pressure, which promoted failure and further permeability increase. The failure of the fault zone conversely enhanced its permeability and contributed to seepage deformation.

Although both mine dewatering or coal mining near fault zones can transform the hydraulic properties of fault zones transform from impermeable to water-conducting, the mechanisms are different (Wu et al. 2011). The mechanism of

water inrush from fault zones disturbed by mining is mainly due to fault zone failure and the increase of pore water pressure because of stress redistribution (Wu et al. 2011; Zhu et al. 2014), while disturbance by mine dewatering is mainly due to feedback effects between the groundwater and fault zone.

To the best of our knowledge, the mechanism of water inrush from fault zones disturbed by mine dewatering is rarely reported (Mu 2018). The results of this study therefore not only provides important information for understanding water inrush from fault zones, but also has practical significance in preventing groundwater inrush events in coal mines.

To prevent water inrush through fault zones disturbed by mine dewatering, dewatering boreholes should, whenever possible, be drilled away from the fault zone. Next, attention should be paid to the mine’s water yield and whether the groundwater contains fine particles in the process of mine inflow. Finally, geophysical prospecting technology should be used to investigate the evolution of fault zones’ hydraulic properties.

Conclusion

The low strength and water sensitivity of media containing clay minerals is the fundamental reason of water inrush along a fault zone disturbed by mine dewatering. The

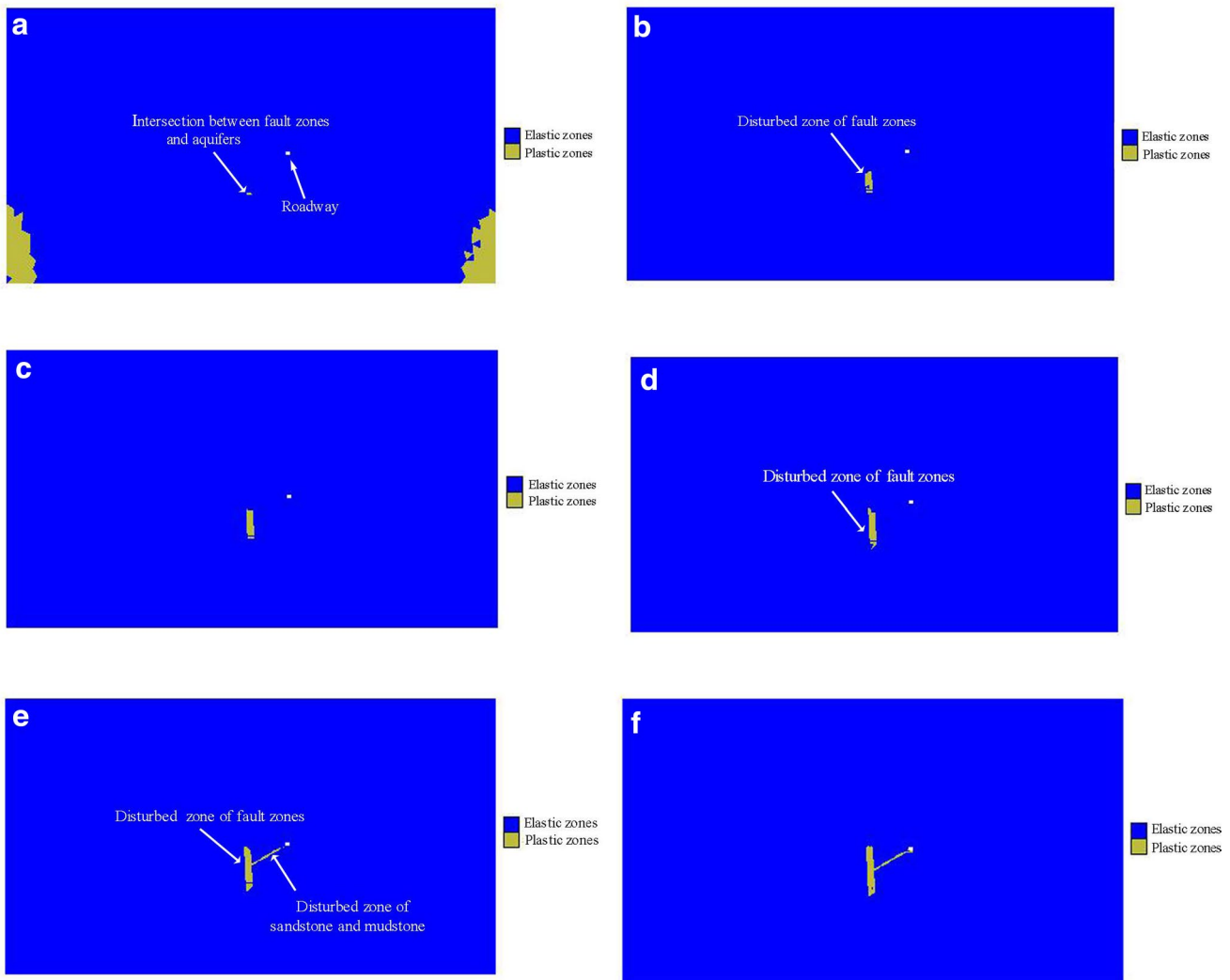


Fig. 13 Plastic zones for different seepage times in the disturbed state: **a** 30 days; **b** 60 days; **c** 90 days; **d** 120 days; **e** 130 days; **f** 160 days

mechanical action and erosive effect of water–rock interactions then promotes water inrush along the fault zone.

The fault zone can be regarded as an almost impermeable medium in its natural state, but transforms into a water-conducting medium due to the feedback effect between the fault zone and groundwater. The numerical model of fluid–solid

coupling presented here considers the effect of mean principal stress and pore water pressure on the permeability of fault zones. Consequently, the model can reveal well the mechanism of water inrush through fault zones disturbed by mine dewatering, and can be used to guide to design a dewatering scheme near fault zones in similar mining areas.

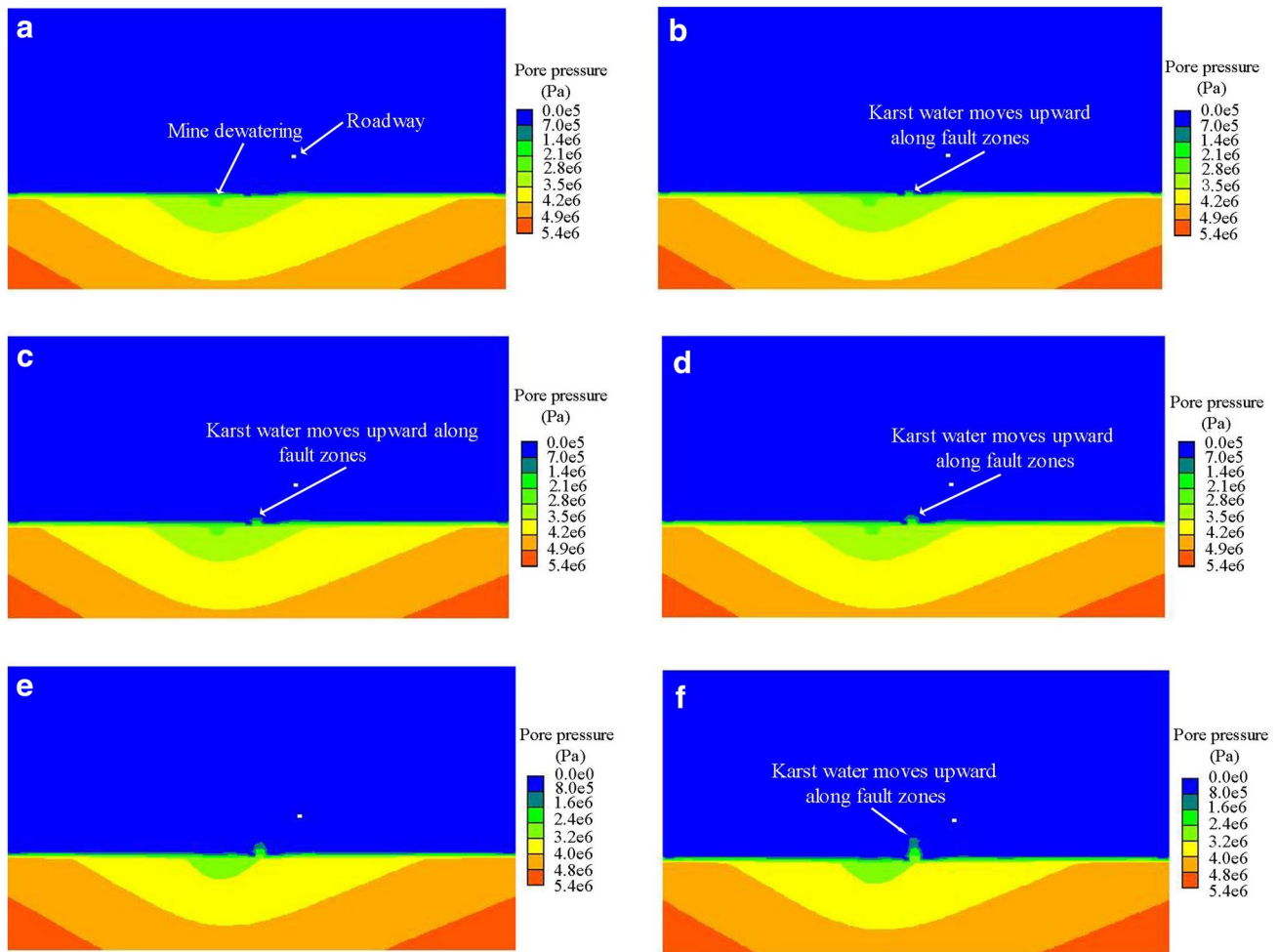


Fig. 14 Pore water pressure for the different seepage time under the disturbed state: **a** 30 days; **b** 60 days; **c** 90 days; **d** 120 days; **e** 130 days; **f** 160 days

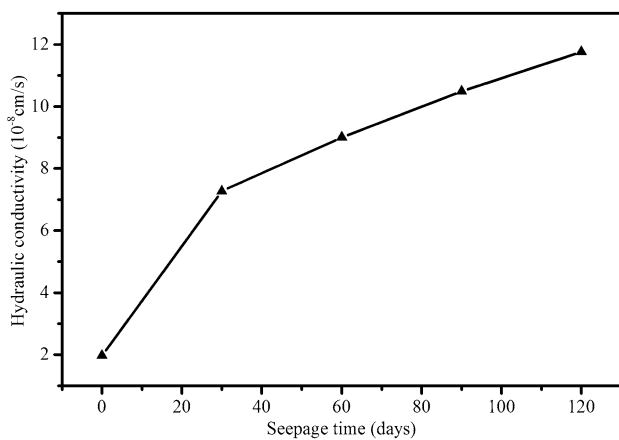


Fig. 15 Permeability variation of fault zones as a function of seepage time in the disturbed state

Acknowledgements This study was financially supported by the China National Scientific and Technical Support Program (Grant 2018YFC0406404) and the National Natural Science Foundation of China (Grant 41572227). The authors also thank the editor and reviewers for their constructive suggestions.

References

Bu WK, Mao XB (2009) Research on effect of fault dip on fault activation and water inrush of coal floor. *Chin J Rock Mech Eng* 28(2):386–394 (in Chinese)

Gui HR, Lin ML (2016) Types of water hazards in China coalmines and regional characteristics. *Nat Hazards* 84(2):1501–1512

Huang CH, Feng T, Wang WJ, Liu H (2010) Research on the failure mechanism of water resisting floor affected by fault. *J Min Safety Eng* 27(2):219–222 (in Chinese)

Jiang ZM, Wang W, Feng SR, Zhong HY (2013) Experimental of study on the relevance between stress state and seepage failure of sandy-gravel soil. *J Hydraul Eng* 44(12):1498–1505 (in Chinese)

- Jiang ZM, Wang W, Feng SR, Zhong HY, Zhao HB (2014) Experimental study on influence of stress state on seepage failure characteristics of coarse grained soil with cohesive particle. *Chin J Geotech Eng* 36(1):98–104 (in Chinese)
- Li B, Wu Q (2019) Catastrophic evolution of water inrush from a water-rich fault in front of roadway development: a case study of the Hongcai Coal Mine. *Mine Water Environ* 38(2):421–430
- Li LJ, Qian MG, Yin YQ (1997) Research on the tests of water inrush from floor simulated by similar materials. *Coal Geol Explor* 25(1):33–36 (in Chinese)
- Li JX, Li DP, Zhang WQ, Liu WT (1999) The relations of initial geostress and water irruption of seam floor. *Chin J Rock Mech Eng* 18(4):419–423 (in Chinese)
- Li XZ, Luo GY, Chen ZS (2002) Mechanism of deformation and water conduction of fault due to excavation in water inrush in underground engineering. *Chin J Geotech Eng* 24(6):695–700 (in Chinese)
- Li LP, Li SC, Shi SS, Xu ZH (2011) Water inrush mechanism study of fault activation induced by coupling effect of stress–seepage–damage. *Chin J Rock Mech Eng* 30(S1):3295–3304 (in Chinese)
- Liu HL, Yang TH, Yu QL, Chen SK (2009) Experimental study on permeability evolution during complete failure process of tuff. *J NE Univ Nat Sci* 30(7):1030–1033 (in Chinese)
- Liu SL, Liu WT, Yin DW (2017) Numerical simulation of the lagging water inrush process from insidious fault in coal seam floor. *Geotech Geol Eng* 35(3):1013–1021
- Ma D, Rezanian M, Yu HS, Bai HB (2016) Variations of hydraulic properties of granular sandstones during water inrush: effect of small particle migration. *Eng Geol* 217:61–70
- Meng ZP, Peng SP, Li H (2001) Influence of normal faults on the physical and mechanical properties of coal and the distribution of underground pressure. *J China Coal Soc* 26(6):561–566 (in Chinese)
- Meng ZP, Li GQ, Xie XT (2012) A geological assessment method of floor water inrush risk and its application. *Eng Geol* 143–144:51–60
- Mu WP (2018) Mechanism of water inrush on faults of coal seam floor and prediction of dewatering rate from karst aquifers in Beiyangzhuang Mine. Diss, China Univ of Mining and Technology, Beijing (in Chinese)
- Qian ZW, Huang Z, Song JG (2018) A case study of water inrush incident through fault zone in china and the corresponding treatment measures. *Arab J Geosci* 11(14):1–17
- Shi LQ, Singh RN (2001) Study of mine water inrush from floor strata through faults. *Mine Water Environ* 20(3):140–147
- Shi WH, Yang TH, Yu QL, Li Y, Liu HL, Zhao YC (2017) A study of water-inrush mechanisms based on geo-mechanical analysis and an in situ groundwater investigation in the Zhongguan Iron Mine, China. *Mine Water Environ* 36(3):409–417
- Sun WB, Zhang SC, Li YY, Lu C (2015) Development of floor water invasion of mining influence simulation testing system and its application. *Chin J Rock Mech Eng* 34(S1):2665–2670 (in Chinese)
- Wang JM, Dong SL, Gong NQ, Gao ZL (1997) Mining disturbance on faults in panel and the hydrogeological effect. *J China Coal Soc* 22(4):361–365 (in Chinese)
- Wang JA, Peng SP, Meng ZP (2001) Permeability rule in full strain-stress process of rock under triaxial compression. *J Univ Sci Technol Beijing* 23(6):489–491 (in Chinese)
- Wang Y, Zhang MS, Hu FS, Ying D, Kun Y (2018) A coupled one-dimensional numerical simulation of the land subsidence process in a multilayer aquifer system due to hydraulic head variation in the pumped layer. *Geofluids* 2018:1–12
- Wu Q, Wang MY (2006) Characterization of water bursting and discharge into underground mines with multilayered groundwater flow systems in the North China coal basin. *Hydrogeol J* 14(6):882–893
- Wu Q, Wang MY, Wu X (2004) Investigations of groundwater bursting into coal mine seam floors from fault zones. *Int J Rock Mech Min Sci* 41(4):557–571
- Wu Q, Zhu B, Liu SQ (2011) Flow-solid coupling simulation method analysis and time identification of lagging water-inrush near mine fault belt. *Chin J Rock Mech Eng* 30(1):93–104 (in Chinese)
- Wu LY, Bai HB, Yuan C, Wu GM, Xu CY, Du Y (2019a) A water-rock coupled model for fault water inrush: a case study in Xiaochang Coal Mine, China. *Adv Civil Eng* 2019:1–12
- Wu Q, Mu WP, Xing Y, Qian C, Shen JJ, Wang Y, Zhao DK (2019b) Source discrimination of mine water inrush using multiple methods: a case study from the Beiyangzhuang Mine, northern China. *Bull Eng Geol Environ* 78(1):469–482
- Xu JP, Zhang FC, Gui H, Zhang TJ (2012) Characteristics and experimental study of water conduction caused by fault activation due to mining. *J China Univ Min Technol* 41(3):415–419 (in Chinese)
- Yin SX, Zhang JC, Liu DM (2015) A study of mine water inrushes by measurements of in situ stress and rock failures. *Nat Hazards* 79(3):1961–1979
- Yin HY, Wei JC, Lefticariu L, Guo JB, Xie DL, Li ZL, Zhao P (2016) Numerical simulation of water flow from the coal seam floor in a deep longwall mine in China. *Mine Water Environ* 35(2):243–252
- Zhang JC (2005) Investigations of water inrushes from aquifers under coal seams. *Int J Rock Mech Min Sci* 42(3):350–360
- Zhang R, Jiang ZQ, Zhou HY, Yang CW, Xiao SJ (2014) Groundwater outbursts from faults above a confined aquifer in the coal mining. *Nat Hazards* 71(3):1861–1872
- Zhang SC, Guo WJ, Sun WB, Li YY, Wang HL (2015) Experimental research on extended activation and water inrush of concealed structure in deep mining. *Rock Soil Mech* 36(11):3111–3120 (in Chinese)
- Zhang PS, Yan W, Zhang WQ, Shen BT, Wang H (2016) Mechanism of water inrush due to damage of floor and fault activation induced by mining coal seam with fault defects under fluid-solid coupling mode. *Chin J Geotech Eng* 38(5):877–889 (in Chinese)
- Zhang SC, Guo WJ, Li YY, Sun WB, Yin DW (2017) Experimental simulation of fault water inrush channel evolution in a coal mine floor. *Mine Water Environ* 36(3):443–451
- Zhou QL, Herrera J, Hidalgo A (2018) The numerical analysis of fault-induced mine water inrush using the extended finite element method and fracture mechanics. *Mine Water Environ* 37(4):1–11
- Zhu WC, Wei CH (2011) Numerical simulation on mining-induced water inrushes related to geologic structures using a damage-based hydromechanical model. *Environ Earth Sci* 62(1):43–54
- Zhu B, Wu Q, Yang JW, Cui T (2014) Study of pore pressure change during mining and its application on water inrush prevention: a numerical simulation case in Zhaogezhuang Coal Mine, China. *Environ Earth Sci* 71(5):2115–2132
- Zhu GL, Zhang WQ, Zhang GB, Wang SL (2017) Experimental study on fault activation conducting water inrush. *Rock Soil Mech* 38(11):90–99 (in Chinese)